

FULL ARTICLE

Development and evaluation of realistic optical cell models for rapid and label-free cell assay by diffraction imaging

Shuting Wang^{1,2} | Jing Liu^{1,2*} | Jun Q. Lu^{1,3} | Wenjin Wang^{1,4} | Safaa A. Al-Qaysi^{3,5} |
Yaohui Xu^{1,2} | Wenhuan Jiang³ | Xin-Hua Hu^{1,3*} 

¹Institute for Advanced Optics, Hunan Institute of Science and Technology, Yueyang, Hunan, China

²School of Information Science and Engineering, Hunan Institute of Science and Technology, Yueyang, Hunan, China

³Department of Physics, East Carolina University, Greenville, North Carolina

⁴School of Physics and Electronic Science, Hunan Institute of Science and Technology, Yueyang, Hunan, China

⁵College of Pharmacy, Al-Mustansiriya University, Baghdad, Iraq

*Correspondence

Xin-Hua Hu, Department of Physics, East Carolina University, Greenville, NC.

Email: hux@ecu.edu

Jing Liu, School of Information Science and Engineering, Hunan Institute of Science and Technology, Yueyang, Hunan.

Email: nameliujing@aliyun.com

Funding information

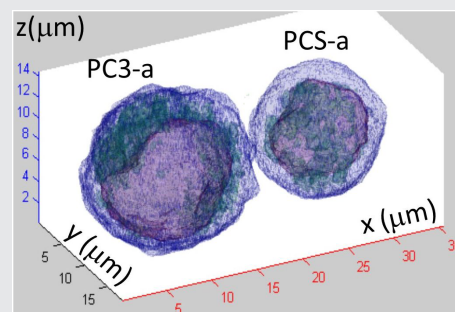
Golfers Against Cancer, Grant/Award Number: 2012-13- GAC; Hunan Provincial Science and Technology Department, Grant/Award Numbers: 2016TP1021, 2018TP2022

Methods for rapid and label-free cell assay are highly desired in life science. Single-shot diffraction imaging presents strong potentials to achieve this goal as evidenced by past experimental results using methods such as polarization diffraction imaging flow cytometry. We present here a platform of methods toward solving these problems and results of optical cell model

(OCM) evaluations by calculations and analysis of cross-polarized diffraction image (p-DI) pairs. Four types of realistic OCMs have been developed with two prostate cell structures and adjustable refractive index (RI) parameters to investigate the effects of cell morphology and index distribution on calculated p-DI pairs. Image patterns have been characterized by a gray-level co-occurrence matrix (GLCM) algorithm and four GLCM parameters and linear depolarization ratio δ_L have been selected to compare calculated against measured data of prostate cells. Our results show that the irregular shapes of and heterogeneity in RI distributions for organelles play significant roles in the spatial distribution of scattered light by cells in comparison to the average RI values and their differences among the organelles. Discrepancies in GLCM and δ_L parameters between calculated and measured p-DI data provide useful insight for understanding light scattering by single cells and improving OCM.

KEYWORDS

cell analysis, cell models, diffraction imaging, light scattering



1 | INTRODUCTION

Biological cells possess heterogeneous and complex 3D morphology to support their functional diversity and environmental adaptability [1]. Study of cell morphology through imaging is of fundamental importance in life science and has been a subject attracting intense research efforts.

Among various imaging options, fluorescence microscopy by incoherent light remains a tool of choice to quantify cell morphology in details. Despite recent advances in microscopy and machine learning [2, 3], these approaches often require staining, time-consuming acquisition and manual reading for interpretation. Alternative methods without staining requirement have stimulated active research interests for the benefits of little disturbance to imaged cells and much

S.W. and J.L. contributed equally to this work.

reduced preparation labors. Compared with other methods, multi-shot and interferogram-based imaging of coherent light scattered by cells stands out for strong signals and its ability to profile 3D distribution of refractive index (RI) [4–10]. Determination of RI distribution from the measured interferogram data, however, requires phase extractions followed by either computationally expensive tomographic reconstruction using, for example, the filtered back projection algorithm [11], or a priori knowledge of cell morphology. Several approximations have been applied in both methods to derive RI that include unwrapping the phase distributions of scattered light treated as scalar wavefields and relating phase data to line integrals of intracellular RI by assuming scattered field as plane wavefields. While validations of these approximations have been performed with simple scatterers such as homogeneous spheres and cells, uncertainty in accuracy of calculated RI remains for the cases of nucleated cells with numerous and highly heterogeneous intracellular organelles of substantially rugged and irregular shapes. The contradictory results on the differences between RI values of cytoplasm and nucleus in previous interferogram based studies manifest such uncertainty in which only cytoplasm and nucleus were considered in light scattering by nucleated cells [8, 10, 12].

Rapid and morphology-based assay through single-shot imaging of coherent light scattered by cells over a limited angular range has been investigated in the settings of flow cytometers and microfluidic devices [13–16]. To achieve high throughput, diffraction imaging needs to be completed in a few milliseconds per cell. Under these conditions, we have developed a method of polarization diffraction imaging flow cytometry (p-DIFC) that acquires a pair of cross-polarized diffraction images (p-DIs) per cell by splitting the scattered light into s- and p-polarized components [17–21]. Unlike quantitative phase imaging methods for RI determination, each p-DI pair by itself provides insufficient “view” of the imaged cell for 3D reconstruction of RI due to the limited angular range of about 50° centered on the side scatter direction. Rather, the goal is to investigate if the p-DI data contain sufficient information for cell assay and classification by light scattering and whether one can correlate the image patterns with the intracellular distribution of RI for extraction of morphology information. It has been shown experimentally that the p-DI pairs contain rich information of diffraction pattern features and allow accurate and rapid classification of cell populations by their strong correlation to 3D morphology [20, 22–26]. These results demonstrate a different and promising approach for accurate, label-free and rapid assay of cells when combined with machine learning-based image processing.

Clear understanding of relations between cell morphology and patterns of acquired images is critically important to translate the p-DIFC method into a practical approach for label-free cell assay. It is very difficult, if not impossible, for

single-shot imaging to measure angular distribution of scattered light reliably over sufficiently large ranges for rapid assay by RI reconstruction. Therefore, development of accurate methodology or framework of modeling and evaluation is necessary to extract useful features from diffraction image (DI) data for morphology based and real-time assay. The challenges for DI simulations are to establish realistic optical cell models (OCMs) and quantify the coherent wavefields of scattered light propagating through imaging optics. Nearly, all reported OCMs up to now have been developed as single or mixed spheres and ellipsoids [27–34]. Other studies have been pursued in modeling light scattering by nonspherical but homogeneous red blood cells and platelets such as biconcave disks, bell-shaped curves, bispheres and over-curved rings [35–39]. While these analytical cell models are useful to illustrate certain aspects of coherent light scattering by cells, they are of very limited capacity to interpret diffraction patterns exhibited by DI data in terms of 3D intracellular distribution of RI related to cell morphology.

Motivated by the lack of accurate tools for nucleated cells of multiple organelles, we have developed tools to reconstruct 3D cellular structures by fluorescent confocal imaging data and convert them into realistic OCMs [18, 40–42]. In this report, we present different realistic OCMs and an evaluation method for detailed comparison of calculated DIs with measured data. A gray-level co-occurrence matrix (GLCM) algorithm has been employed to quantify textures of measured and calculated DIs. The dependence of GLCM parameters extracted from calculated p-DI pairs on cell morphology and RI distribution was analyzed with four types of OCMs built with two prostate cell structures. We show by these results that the new method by quantitative comparison of diffraction patterns in p-DI data allows development and improvement of realistic OCMs for morphology-based cell assay by single-shot diffraction imaging.

2 | METHODS

2.1 | Measurement and calculation of p-DI pairs

For acquisition of p-DI pairs from single cells, suspension samples of biological cells are prepared in a concentration of about 2×10^6 cells/mL and injected into the core fluid stream of a p-DIFC system [17–20, 24]. A continuous-wave and linear polarized laser beam of $\lambda = 532$ nm in wavelength is propagated along the z-axis and focused on the core fluid. By hydrodynamic focusing with a sheath fluid, cells flow in a single file through the focal spot of incident beam that is about the size of core fluid around $30 \mu\text{m}$. Light scattering occurs as the cell passed through the focus of incident beam due to the mismatch of RI between cell and core fluid as host medium. The coherent light scattered by the cell propagates through the host medium of water and a glass

flow chamber before collection by an imaging unit along the side directions as shown in Figure 1A. The imaging unit detailed in Figure 1B consists of an infinity-corrected 50x objective of 0.55 in NA (378–805-3, Mitutoyo, Aurora, Illinois), a polarizing beam splitter for separating scattering light into s- and p-polarized components, two tube lenses and two charge-coupled-device (CCD) cameras. The unit, with camera sensor fixed to the focal plane of tube lens, can be translated away from the focused position toward the flow chamber ($\Delta x > 0$) to increase the contrast and vary collection angular cone [18, 43].

The diffraction imaging process using a p-DIFC systems is simulated by a hybrid model according to the experimental configuration illustrated in Figure 1A. [17–20]. Briefly, the calculated p-DI pairs are obtained in two steps: simulation of light scattering by a cell presented as an OCM followed by ray-tracing based on geometric optics through the assembly of host medium of water, chamber glass, air and imaging unit. An open-source code of ADDA allows accurate simulation of the coherent scattering using the discrete-dipole-approximation [44]. In this method, an incident laser beam is represented by a plane wavefield and the cell as a scatterer by a voxel array of OCM with heterogeneous intracellular RI distribution. The angle-resolved distributions of scattered light intensity are saved in the form of 4×4 Mueller matrices $[S_{ij}(\theta_s, \phi_s)]$ with (θ_s, ϕ_s) as the scattering polar and azimuthal angles [36]. A code for relaying scattered light from the scatterer at the origin to camera sensor has been built on MATLAB (2013a, MathWorks, Natick, Massachusetts) for geometric optics-based ray-tracing. The software first reads selected elements of S_{ij} based on the polarizations of

incident and scattered light and project them on a virtual input plane Γ_{in} indicated in Figure 1B as an input image $I_{in}(z, y)$. The pixels of I_{in} are associated with the rays of scattered light propagating along directions marked by $\theta_s \in [65^\circ, 115^\circ]$ and $\phi_s \in [160^\circ, 200^\circ]$ [22]. The MATLAB code then calls a commercial software (2009, Zemax, Kirkland, Washington) to perform ray-tracing from $I_{in}(z, y)$ on Γ_{in} from the host medium of water to the image plane Γ_{im} at the end of imaging unit to obtain a calculated image of $I_{im}(z, y)$ on Γ_{im} as illustrated in Figure 1B. Different sets of the Mueller matrix elements S_{ij} need to be used for different combinations of incident beam polarization and s- or p-polarized DIs with details given in [42].

2.2 | Optical modeling of single cells

To build realistic OCMs with 3D structures, we acquire confocal fluorescent image stacks of doubly stained cells as described elsewhere [41, 45]. The cells are typically stained with Syto-61 for nucleus and MitoTracker Orange for mitochondria due to their important roles in light scattering [46, 47]. The fluorescence intensity of the two reagents is recorded in red and green channels as $F_r(\mathbf{r})$ and $F_g(\mathbf{r})$, respectively. Reconstruction is performed by an in-house developed MATLAB code on a confocal image stack by segmentation of each raw image slice followed by slice interpolation to obtain an array of cubic voxels representing the cell's 3D morphology. The exported voxel array contains organelle type identifier for each voxel, cytoplasm or nucleus or mitochondria, and the fluorescence intensity of $F_r(\mathbf{r})$ and $F_g(\mathbf{r})$ [45]. For this study, the nuclear (or mitochondrial) voxels carry F_r (or F_g) values only while the cytoplasm voxels hold both intensities as the result of target molecules existing in small concentrations in cytoplasm. Each cell structure has an orientation vector \mathbf{C} defined as a line pointing from the mass center of cell to that of nucleus that has its Euler angles given by (α, β, γ) in the coordinate system defined in Figure 1.

A realistic OCM is defined in the near-field zone simulation of light scattering by ADDA using the 3D voxel array described above. Each intracellular voxel at \mathbf{r} has its real part values of complex RI denoted as $n_\eta(\mathbf{r})$ with $\eta = c$ or n or m for cytoplasm or nucleus or mitochondria, respectively. The voxels external to the cell in the near-field zone are regarded as the host medium of water for ADDA calculation and their real part values of RI are set to $n_h = 1.334$ for light of $\lambda = 532$ nm. For prostate cells described in this study, we consider them having little absorption in the visible spectral region so that the imaginary part values of RI are set to 1.5×10^{-5} for all voxels. The ADDA simulations were performed with ratios of wavelength-to-voxel-size or dipole-per-wavelength (dpl) values ranging from 5 to 10 [44].

We have developed fluorescence intensity-based OCMs to obtain $n_\eta(\mathbf{r})$ for intracellular voxels [41]. In this model, the concentrations of molecules targeted by the fluorescent reagents are presumed to be linearly proportional to $F_r(\mathbf{r})$ or $F_g(\mathbf{r})$. Furthermore, we assume a linear relation between the

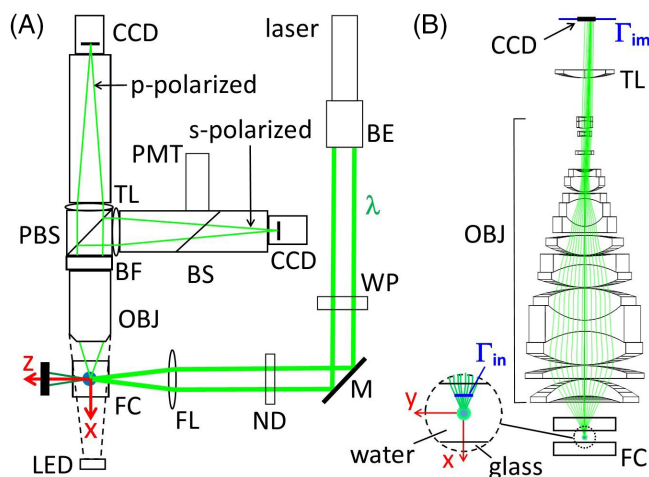


FIGURE 1 A, schematic of polarization diffraction imaging flow cytometry (p-DIFC) configuration with the green lines representing incident and scattered light of $\lambda = 532$ nm and red lines the coordinate axes: BE = beam expander; M = mirror; ND = neutral density filter; FL = focusing lens; FC = flow chamber; LED = white illumination LED; OB = objective; BF = bandpass filter centered at 532 nm; PBS = polarizing beam splitter; BS = beam splitter; TL = tube lens; CCD = camera. B, schematic of cross-polarized diffraction image (p-DI) simulation along one polarized branch with blue lines representing the input plane Γ_{in} and image plane Γ_{im}

dry mass of a targeted molecule type in each voxel with real RI given by

$$n_{\eta}(\mathbf{r}) = n_{c0} + b_r F_r(\mathbf{r}) + b_g F_g(\mathbf{r}) \quad \forall \mathbf{r} \in \Omega_{\eta}, \quad (1)$$

where n_{c0} is the RI of aqueous component in organelles such as cytosol in cytoplasm, b_r or b_g is respectively the specific RI increment coefficients by concentration or dry mass per voxel and Ω_{η} represents the voxel set of organelle η . The two coefficients of b_r and b_g thus link fluorescent light intensity recorded in the confocal image to the concentrations of nuclear acids and mitochondrial biomolecules targeted by the reagents. The fluorescence intensity based OCMs as given by Equation (1) are denoted as OCM_{η} in this report, and the three parameters of n_{c0} , b_r and b_g can be adjusted to examine the effects of organelle molecules on diffraction patterns embedded in p-DI pairs. It is easy to show that b_r is determined by the average RI of nuclear voxels or $n_{n,av}$ with the aid of Equation (1) by summing over all nuclear voxels, that is,

$$n_{n,av} = n_{c0} + b_r \left\{ \frac{1}{N_n} \sum_{\mathbf{r} \in \Omega_n} F_r(\mathbf{r}) \right\} = n_{c0} + b_r F_{m,av}, \quad (2)$$

where $F_{m,av}$ is the average Syto-61 fluorescence intensity saved in red channel for all nuclear voxels. With the above result, we find

$$b_r = \frac{n_{n,av} - n_{c0}}{F_{m,av}}. \quad (3)$$

Similarly, one can derive b_g from $n_{m,av}$ by

$$b_g = \frac{n_{m,av} - n_{c0}}{F_{gm,av}}, \quad (4)$$

with $F_{gm,av}$ as the average fluorescence intensity of MitoTracker Orange saved in green channel for all mitochondrial voxels. The ‘‘molecular composition’’ of a given OCM_{η} based on a cell structure can be modified by adjusting the input parameters of n_{c0} , $n_{n,av}$ and $n_{m,av}$.

Three variants of OCM_{η} are introduced in this study to investigate the effect of RI heterogeneity on DIs with the same set of input parameters. Two of these models denoted as OCM_{pfn} and OCM_{pfm} are of ‘‘partial fluorescence’’ nature in which voxels of only one organelle type, nucleus or mitochondrion, have their RI values obtained by Equation (1) while the voxels of the other two organelle types are set to have constant RIs. For example, OCM_{pfn} has $n_{\eta}(\mathbf{r})$ given by Equation (1) and $n_c(\mathbf{r}) = n_{c,av}$ and $n_m(\mathbf{r}) = n_{m,av}$. The last model is defined as OCM_{nf} of ‘‘no fluorescence’’ nature in which the RI values are set to different constants as $n_c(\mathbf{r}) = n_{c,av}$, $n_m(\mathbf{r}) = n_{m,av}$ and $n_n(\mathbf{r}) = n_{n,av}$.

2.3 | Quantitative image characterization by GLCM parameters

As a second-order statistical method, the GLCM algorithm generates a matrix $p(d, \xi) = [p_{ij}(d, \xi)]$ of rank G given an input image I and G is the number of gray levels or pixel

intensities of I [48]. Each element $p_{ij}(d, \xi)$ is defined as the relative frequency of pixel pairs having intensities of i and j and the two pixels in each pair are separated by d pixels along a direction marked by ξ . Four matrices can be obtained for the four directions of pixel pairs with $\xi = 0^\circ, 45^\circ, 90^\circ$ and 135° . In this study, we employed the GLCM averaged over the four directions with $d = 1$ for each input image. Before GLCM calculation, an image I of 12-bit pixels in a measured p-DI pair or of 16-bit pixels in a calculated p-DI pair was normalized into 8-bit pixels so that the GLCM of rank G equals to 2^8 or 256 for reduced computational cost. The image textures are quantified by 15 parameters extracted from the averaged GLCM whose definitions and symbols are given in [49].

3 | RESULTS AND DISCUSSION

3.1 | Confocal imaging of PC3 and PCS cells

Two prostate cell types were used for this study: PC3 human prostate cancer cells (CRL-1435, ATCC, Manassas, Virginia) and PCS normal human prostate epithelial cells (PCS440010, ATCC). A total of 40 PC3 and 38 PCS cells doubly stained by Syto-61 and MitoTracker Orange were imaged with a laser scanning confocal microscope (LSM 510, Zeiss, Thornwood, New York) [24]. Image stacks were acquired using a 63 \times water-immersion objective of 1.2 in NA and a 4 \times digital zoom. Figure 2A,B present confocal image slices selected from the stacks of a PC3 and a PCS cell acquired with a stepsize of 0.5 μm along the direction perpendicular to the object plane. For each image slice of 512 \times 512 pixels, the fluorescence light intensities of Syto-61 saved in red and MitoTracker Orange in green channels were used to segment pixels into three sets of nucleus, mitochondria and cytoplasm. Then additional slices were added through interpolation for reconstruction of a 3D array of nearly cubic voxels and calculation of 29 morphology parameters [41, 45]. We have performed diffraction imaging simulations on six cell structures with three for each of the PC3 and PCS types that have typical morphology parameters among the imaged cells. The results presented in this report were obtained with two of the six cell structures denoted as PC3-a and PCS-a in Figure 2C and Table 1. We note that the size of PC3-a cell is significantly larger than that of the PCS-a cell, which allow us to compare the effect of different morphology on textures and GLCM parameters of the calculated DIs.

3.2 | Diffraction imaging of PC3 and PCS cells and GLCM parameter correlations

We acquired p-DI pairs of 640 \times 480 pixels for each image from PC3 and PCS cells using a p-DIFC system and an incident laser beam of $\lambda = 532$ nm [24]. The imaging unit was translated to an off-focus distance of $\Delta x = 150$

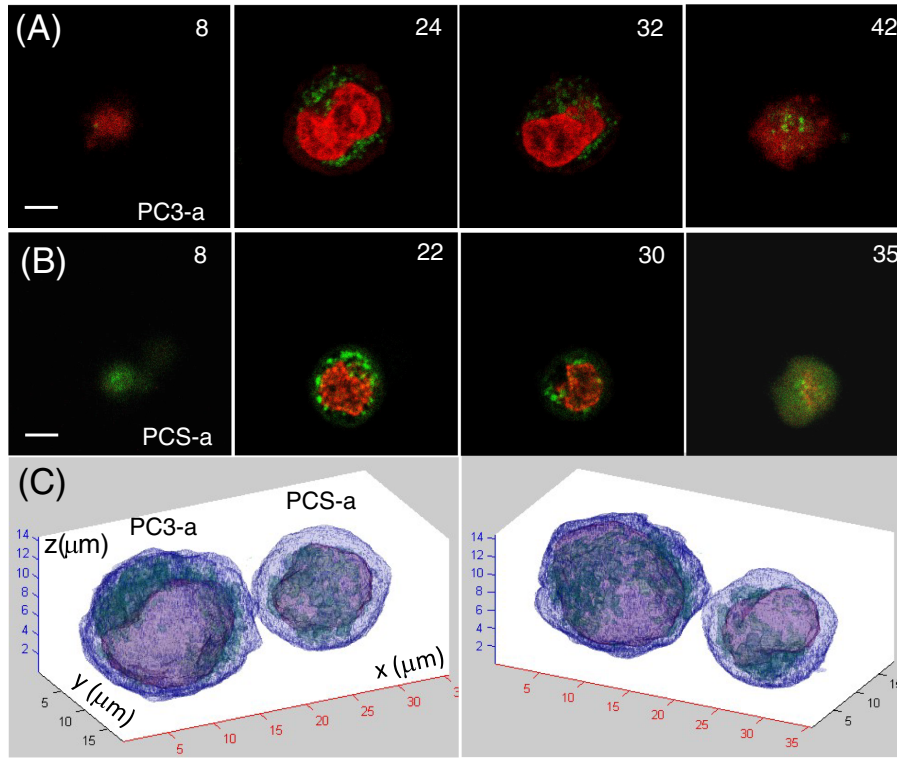


FIGURE 2 Selected confocal images acquired from the following: A, a PC3 cell and B, a PCS cell marked with slice numbers in respective stack. The red and green channels store Syto-61 and MitoTracker Orange intensities respectively. C, two perspective views of the two reconstructed cells with nuclei colored in dark pink and mitochondria in green. Bar = 5 μm

TABLE 1 Three-dimensional morphology parameters of PC3-a and PCS-a cells^a

Cell structure ID	V_c (μm^3)	SVr_c (μm^{-1})	ER_c (μm)	$\langle R_c \rangle$ (μm)	Vr_{nc} (%)	SVr_n (μm^{-1})	Vr_{mc} (%)	SVr_m (μm^{-1})
PC3-a	2250	0.500	8.13	8.35	44.0	0.693	5.57	6.24
PCS-a	1118	0.614	6.44	6.56	30.1	0.964	4.71	6.42

^a ID: identification; V_c : cell volume; SVr_c (SVr_n or SVr_m): surface-to-volume ratio of cell (nucleus or mitochondrion); ER_c : equivalent radius of cell; $\langle R_c \rangle$: average distance of cell membrane voxels to centroid; Vr_{nc} (Vr_m): volume ratio of nucleus(mitochondrion)-to-cell.

μm for increasing the angular magnification of scattered light as discussed in [43]. The direction of linear polarization was changed for the incident laser beam during data acquisition to be either vertical (ver), horizontal (hor) or 45° from horizontal z-axis in the scattering plane (x-z). In Figure 3 we present examples of measured p-DI pairs acquired with three different incident beam polarizations, which are used here for comparison to the calculated p-DI pairs. To quantify the transfer of light energy between co-polarized and cross-polarized components, we employed the linear depolarization ratio as defined below [50].

$$\delta_{L,ver} = \frac{\bar{I}_{p,ver}}{\bar{I}_{s,ver}}, \quad \delta_{L,hor} = \frac{\bar{I}_{s,hor}}{\bar{I}_{p,hor}}, \quad \delta_{L,45^\circ} = \frac{\bar{I}_{p,45^\circ}}{\bar{I}_{s,45^\circ}}, \quad (5)$$

where \bar{I} is the average pixel intensity of an image with its subscripts indicating the polarizations of incident and scattered light. Table 2 provides the values of linear depolarization ratio and other parameters for one set of measured data. The mean values of δ_L show that these cells exhibit

strong ability to transfer energy in the side scatter from co-polarized to cross-polarized component relative to the incident light. In comparison, single particles of spherical symmetry have $\delta_{L,ver} = \delta_{L,hor} = 0$.

Using the measured p-DI data of PC3 and PCS cells, we further assessed GLCM parameter correlations in search of a small set that has sufficient information capacity for texture characterization. Otherwise, employment of all 15 GLCM parameters presents a high dimensional problem that often obscures the evaluation of OCMs. A total of 7322 DIs from three sets of p-DI pairs measured from PC3 and PCS cells were used to calculate the 15 GLCM parameters after normalization into eight-bit images. Bivariate Pearson and Spearman correlation coefficients [51] were obtained on paired GLCM parameters and are denoted, respectively, as r_p and r_s . Their values range from less than 0.1 for very weak correlations to larger than 0.9 for very strong correlations for a given pair of GLCM parameters. In addition to $|r_p|$ and $|r_s|$, we also obtained the multiple correlation coefficient R^2 using the same combined DI data set to assess each GLCM parameter's predictability of the

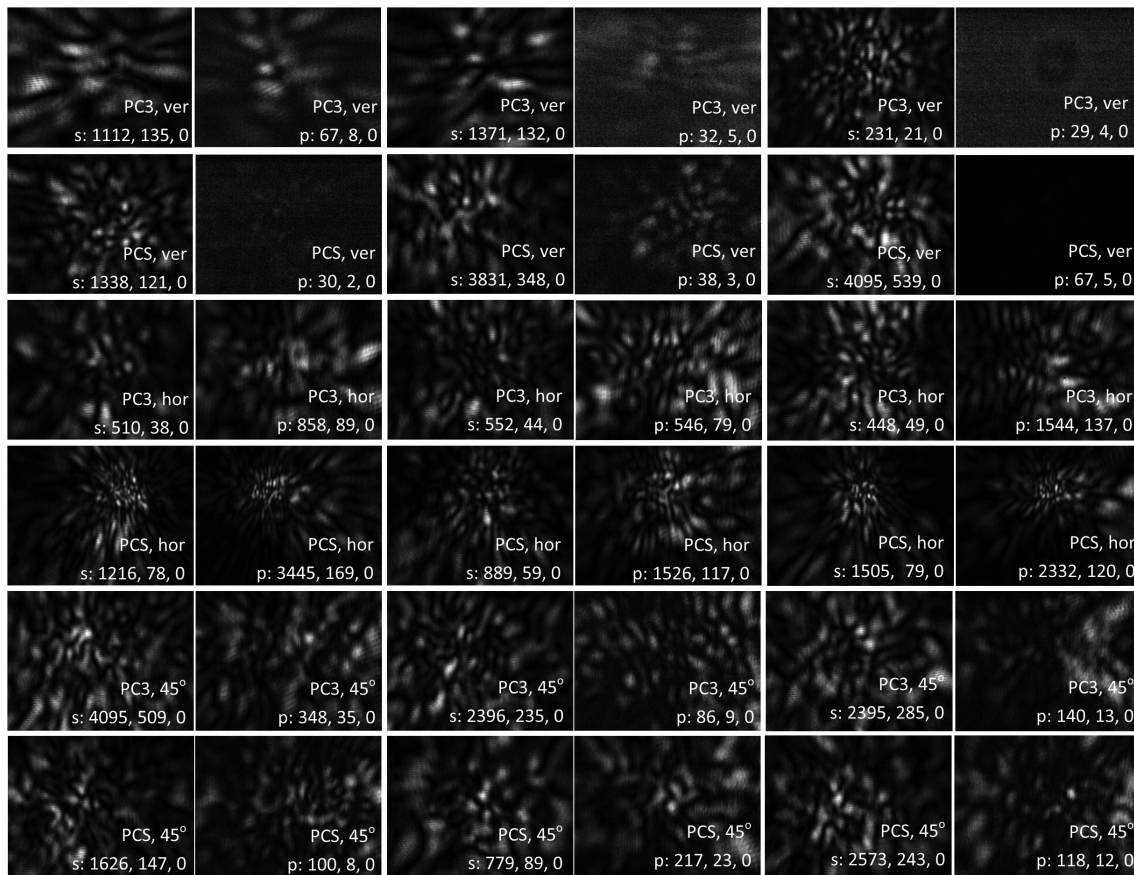


FIGURE 3 Selected cross-polarized diffraction image (p-DI) pairs acquired from single PC3 and PCS cells and normalized by each image's maximum and minimum pixel values. The cell type, incident beam polarization, scattered light polarization (s or p), maximum, average and minimum pixel values are marked in each image

other 14 parameters in their values. The ranked list of GLCM parameters is given in Table 3 in the order of increasing R^2 values.

We chose a set of four parameters for OCM evaluation here that consists of the top three parameters of low R^2 values and one of good performance in classifying PC3 and PCS cells by the support vector machine method [24]. Figure 4 presents the scattered plots of these GLCM parameters in pairs with values of r_p and r_s . It can be seen from these plots that the DIs of PC3 cells have their parameter values clustered near the low ends of ranges for each of the four parameters in comparison with those of PCS cells.

3.3 | Calculated p-DI pairs: Effect of cell orientation

Calculations of p-DI pairs were carried out with different OCMs and the simulation method described in the Method section with $\lambda = 532$ nm and other parameters based on the experimental configuration. As nonspherical and highly heterogeneous scatterers, a biological cell is expected to yield different spatial distributions of scattered light as its orientation changes relative to the incident beam. Based on our experimental and numerical study results, however, the orientation variations among cells imaged by the p-DIFC method do not prevent cell classification into different prototypes [20, 22, 24, 25] or OCMs in different RI distributions [42]. This suggests that in a flow cytometry setting

TABLE 2 The values of linear depolarization ratio δ_L and other parameters

Parameters	PC3 cells			PCS cells		
	ver	hor	45°	ver	hor	45°
Incident power P_0 (mW)	41	89	73	41	89	73
Number of p-DI pairs N_{DI}	716	681	770	668	623	378
Pixel intensity $\bar{I}_s, \bar{I}_p^{(a)}$	177,4.90	40.3,97.2	310.2,13.7	336,18.5	77.2197	286,16.8
Maximum δ_L (%)	22.9	109	23.3	253	602	51.2
Minimum δ_L (%)	1.81	11.7	2.16	0.356	4.58	2.70
Mean δ_L (%)	3.05	45.6	4.30	5.92	61.0	5.96

Abbreviations: p-DI, cross-polarized diffraction image; hor, horizontal; ver, vertical.

TABLE 3 The list of 15 GLCM parameters ranked by increasing R^2 values

GLCM parameters	ASM ^a	ENT	MAP	COR	CLP	CLS	SVA	VAR
R^2 (%)	97.95	98.98	99.04	99.34	99.41	99.77	99.78	99.78
GLCM parameters	SEN	CON	DEN	SAV	IDM	DVA	DIS	
R^2 (%)	99.81	99.82	99.84	99.84	99.84	99.94	99.95	

^a GLCM parameter definition is given in [49].

Abbreviation: GLCM, gray-level co-occurrence matrix.

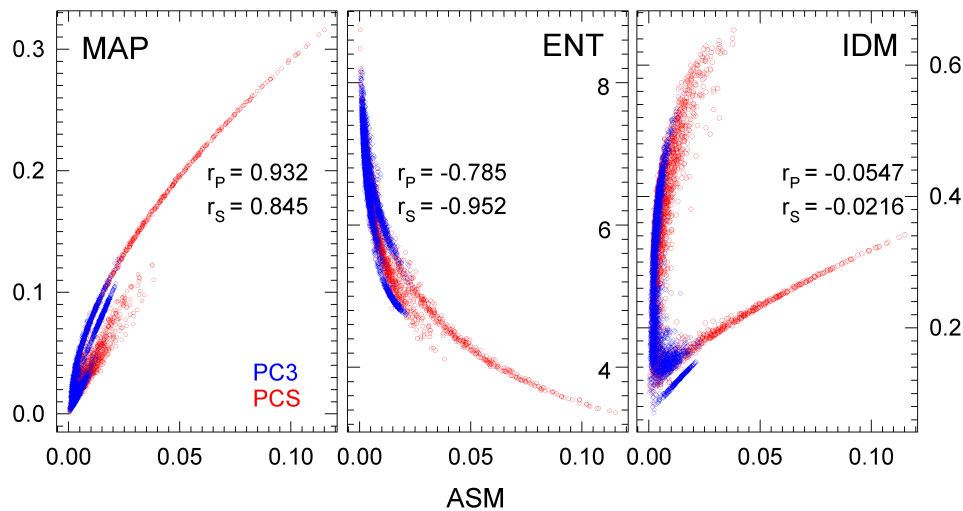


FIGURE 4 Scattered plots of four gray-level co-occurrence matrix (GLCM) parameters extracted from diffraction images of 4520 PC3 and 2802 PCS cells: ASM = angular second moment; MAP = maximum probability; ENT = entropy; IDM = inverse difference moment. The values of r_P and r_S are given in each plot

orientation is likely not randomized among imaged cells but rather aligned in certain preferred directions. To verify this conclusion, we calculated p-DI pairs by the PC3-a and PCS-a structures and $OCM_{\vec{n}}$ defined in Equation (1). Each cell structure has been rotated 12 times by varying the Euler angles of vector \mathbf{C} and the off-focus distance Δx of the imaging unit was set to $80 \mu\text{m}$ in ray-tracing for larger angular ranges of scattered light collection in calculated p-DI data. Figure 5 presents four examples of the calculated p-DI pairs for each cell structure with the vertical incident polarization for comparison of image pattern changes. By visualization and comparison of GLCM parameters (not shown) and $\delta_{L, \text{ver}}$, we found the texture and pixel intensity changes due to varied cell orientation are relatively small in comparison to fluctuations in the measured data as shown in Figure 3 and the values of δ_L in Table 2. In the following results, we compare different OCMs at a fixed orientation by setting all OCMs at the same direction of \mathbf{C} that corresponds to $(\alpha, \beta, \gamma) = (0, 0, 0)$ unless noted otherwise.

3.4 | Calculated p-DI pairs: Effect of OCMs

We performed p-DI simulations with four types of OCMs built from prostate cell structures of PC3-a and PCS-a for each of three incident beam polarizations. The results presented here are mainly on the variation of the average RI value $n_{n, \text{av}}$ for nuclear voxels between 1.390 and 1.470 in

steps of 0.020 while n_{c0} and $n_{m, \text{av}}$ were fixed at 1.360 and 1.530. The choice of these RI value ranges was based on results published in literature [5, 7, 9] and so did other choices of RI parameter value including different values of $n_{m, \text{av}}$. The off-focus distance Δx of the imaging unit in ray-tracing calculations was changed to $150 \mu\text{m}$, which is the same value used for p-DI measurement to facilitate the comparison of calculated and measured data. The wall-clock time T of light scattering simulation depends on the size of cell structures and choices of RI values for parallel execution of ADDA code on 24 CPU cores of a computing cluster node (PowerEdge C4130, Dell, Round Rock, Texas). For PCS-a of small cell size and same values of n_{c0} at 1.36 and $n_{m, \text{av}}$ at 1.530, T ranges from about 24 for $n_{n, \text{av}} = 1.39$ to 32 minutes for $n_{n, \text{av}} = 1.47$ while T ranges from 61 to 387 minutes for PC3-a of large size and the same RI variations. Compared to ADDA simulation, projection of the Mueller matrix elements to the input plane Γ_{in} and ray-tracing to the image plane Γ_{in} took only around 10 minutes on a computer with one i5-6500 CPU of 3.2GHz.

Figures 6 and 7 show examples of calculated p-DI pairs with vertical and horizontal incident beam polarizations that are analyzed in detail below. By comparing the calculated p-DI pairs in these two figures to the measured data in Figure 3, certain similarity in image textures can be identified to support the use of realistic OCMs as defined in this report for simulation of diffraction imaging. We note further that the

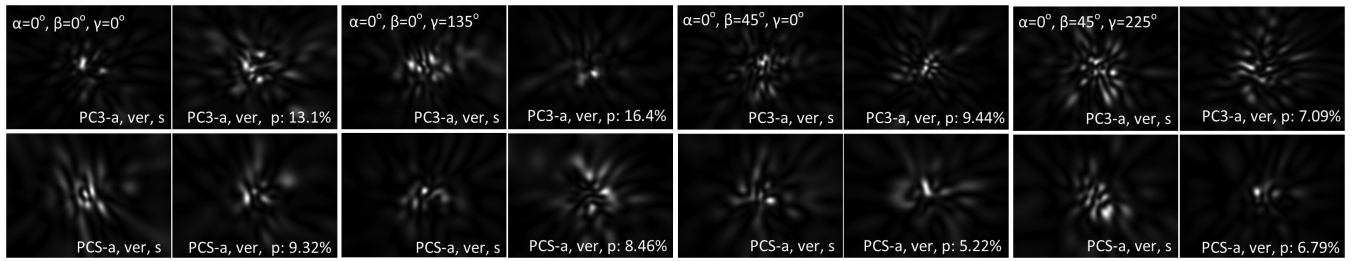


FIGURE 5 Normalized cross-polarized diffraction image (p-DI) pairs calculated by optical cell model (OCM)_{fl} with two cell structures with vertical incident polarization, $\lambda = 532$ nm and $\Delta x = 80$ μ m. Each pair is marked with Euler angles of C, cell structure, incident and scattered polarizations and value of δ_L . Refractive index (RI) parameters are given by $n_{c0} = 1.360$, $n_{n,av} = 1.390$ and $n_{m,av} = 1.530$

OCMs with the chosen RI parameter values yield values of linear depolarization ratio or δ_L , as marked in Figures 6 and 7, close to those of measured DIs as listed in Table 2. Specifically, significant differences in δ_L values of p-DI pairs between ver and hor incident polarizations can be found in the calculated data that $\delta_L \sim 10\%$ for DIs in Figure 6 with ver incident polarization and increases by factors up to three for DIs in Figure 7 with hor polarization. The same relation with large factors of increase also occurs in the measured data as shown in the Table 2 data.

For quantitative evaluation, we applied the GLCM algorithm for characterization of image textures with four parameters selected for their different capacities to depict image textures and high performance to classify PC3 and PCS cells by the measure DI data. We plot in Figures 8 and 9 the dependence of GLCM parameters on average nuclear voxel RI value $n_{n,av}$ in the four OCM types for ver and hor incident polarizations. Each symbol with the associated error bar represents the mean value and SD of a GLCM parameter from one DI calculated by the same OCM in three orientations, which allow the estimation of fluctuations in DI data due to small variation of cell orientation in passing through the incident beam. Consistent with the results in Figure 5, the

GLCM parameter fluctuations revealed by the error bars show the effect of cell orientation on diffraction patterns. The fact that accurate cell classification can be achieved by the measured p-DI data [24] suggest that the differences in intracellular distribution of RI dominate the spatial distribution of scattered light in comparison with the orientation variations.

It is first noticed only in the case of PC3-a for a large cell structure with incident polarization of ver that the OCM_{nf} model of constant but different organelle RI values yields GLCM parameters significantly different from the other three OCMs when $n_{n,av}$ increases to 1.470. The deviation of GLCM parameters of DIs by OCM_{nf} from the other models disappears in other cases of PCS-a as a smaller cell structure and hor polarization as shown by the diagrams on the right column of Figure 8 and both columns of Figure 9. Similar results were also observed in OCMs with small values of $n_{m,av}$ for mitochondrial voxels ranging from 1.410 to 1.590 (not shown). These results suggest that the heterogeneity in RI values of nuclear voxels can significantly modify the textures of DIs for large nuclear volume V_n which diminishes as V_n decreases. The GLCM parameter data in Figures 8 and 9 also demonstrate that the diffraction patterns in the

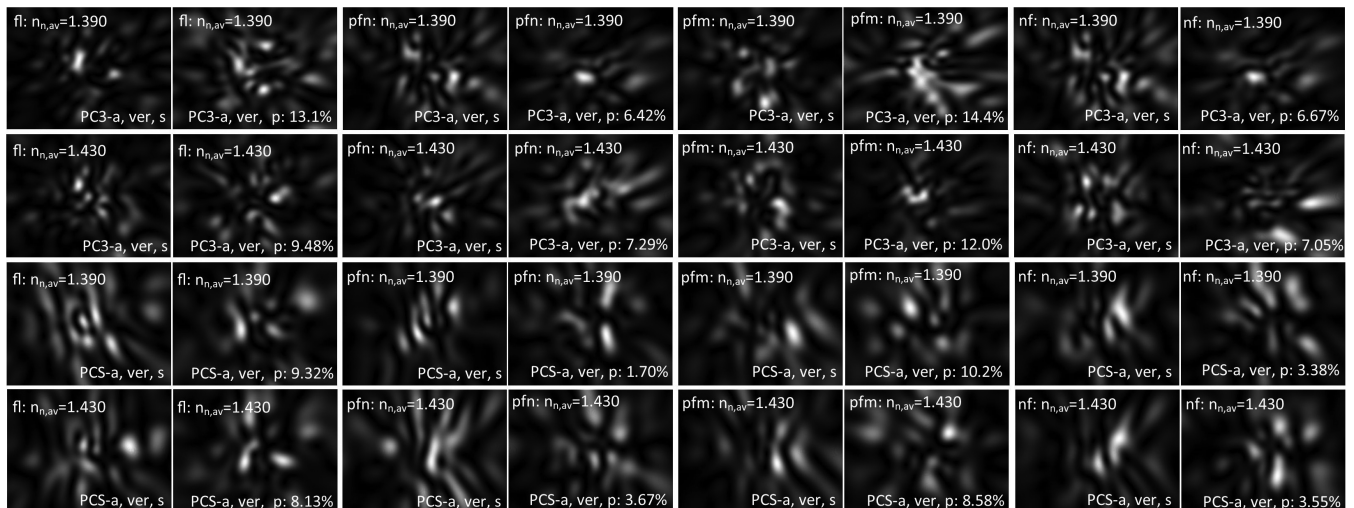


FIGURE 6 Normalized cross-polarized diffraction image (p-DI) pairs calculated by different optical cell models (OCMs) ranging from OCM_{fl} on the two left columns to OCM_{nf} on the two right columns with vertical incident polarization, $\lambda = 532$ nm and $\Delta x = 150$ μ m. Each pair is marked with OCM type, $n_{n,av}$, cell structure, incident and scattered polarizations and value of δ_L . Other refractive index (RI) parameters are given by $n_{c0} = 1.360$ and $n_{m,av} = 1.530$

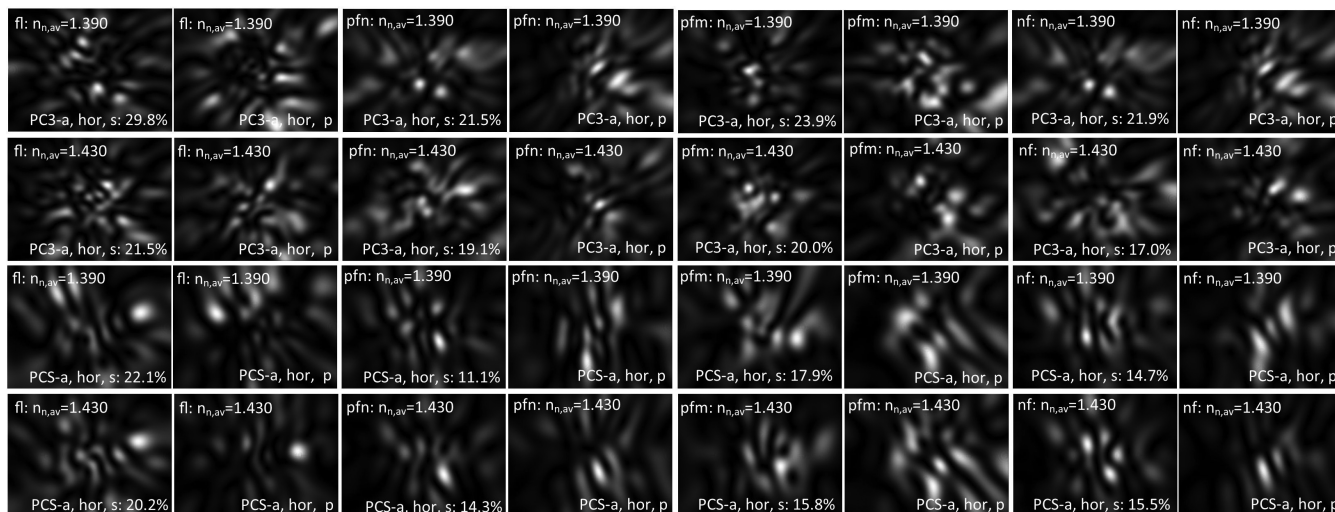


FIGURE 7 Same as Figure 6 except with horizontal incident polarization

calculated DIs are not sensitive to the values of average nuclear RI, which is corroborated by direct examination of DIs in Figures 6 and 7. Furthermore, both of the measured and calculated DI data presented in this report exhibit highly unsymmetrical diffraction patterns that are entirely different from those in DIs of single and aggregated spheres [26, 52]. Taken together, these results indicate strongly that the highly

irregular shapes of and RI heterogeneity inside organelles play more important roles than the average RI values in the spatial distribution of scattered light wavefields.

Even though GLCM parameters are difficult to interpret, it is possible to gain useful insights from their definitions for evaluation of OCMs by analyzing the value differences between calculated and measured DIs [48, 49]. For example,

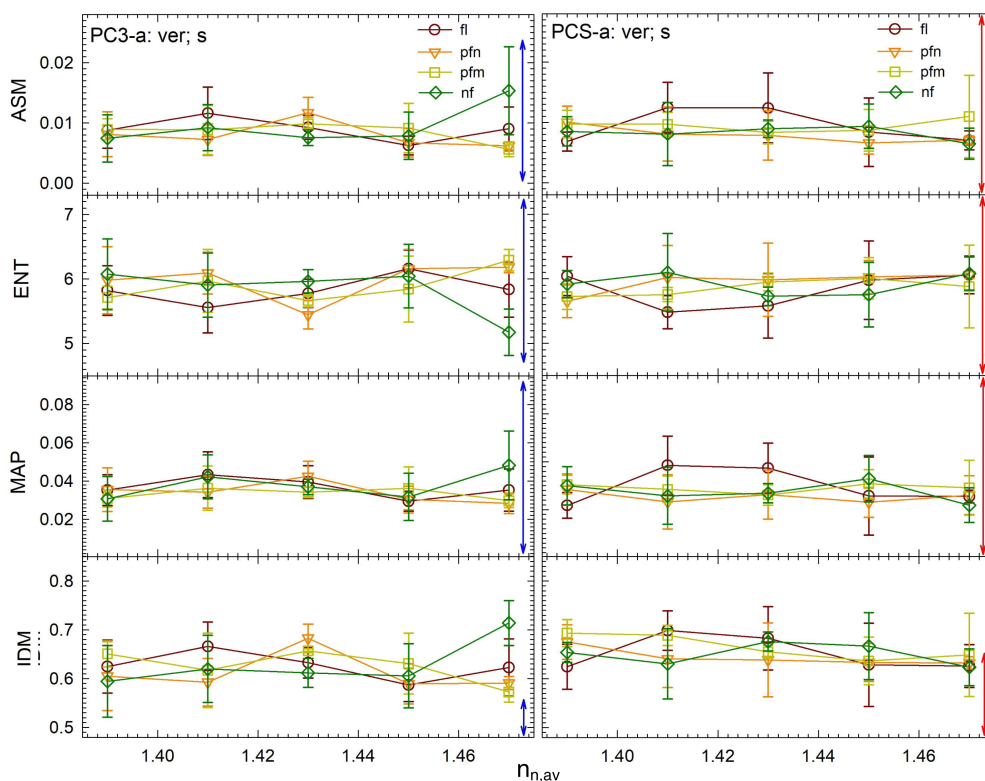


FIGURE 8 Selected four gray-level co-occurrence matrix (GLCM) parameter of s-polarized diffraction images (DIs) and vertical incident polarization vs $n_{n,av}$ in different optical cell models (OCMs) of PC3-a (left column) and PCS-a (right column) with simulation parameters given in Figure 6. Each symbol and error bar represent the mean value and SD determined from DIs obtained using the same OCM in three orientations with Euler angles of C given by (0, 0, 0), (0, 30°, 0) and (0, 0, 30°). The arrowed vertical lines on the right indicate the parameter ranges of the measured data shown in Figure 4 for the same cell type. The lines connecting symbols are for visual guide

ASM or angular second moment is obtained as the sum of squared elements as p_{ij}^2 and varies between G^{-2} and 1. For $G = 256$ in our cases this leads to $1.53 \times 10^{-5} \leq \text{ASM} \leq 1$. For images of increasingly randomized pixel intensity, ASM value decreases because p_{ij} approaches to a constant of G^{-2} . The ASM value increases toward 1 for images of periodic variations in pixel intensity and become 1 if the period equals to the paired pixel distance d . Consequently, the value of ASM offers a measure of randomness in paired pixel intensity distributions. Because of the noise background in measured DIs as shown in Figure 3, one can expect that the ASM values for these images tend to be smaller than those in the calculated ones in Figures 6 and 7. This turns out to be the case for calculated DIs with OCMs using the PC3-a structure that stay near the low end of the range of the measured data as indicated by the arrowed line. One may attribute the better matches between ASM values of calculated and measured DIs in the case of PCS-a to the fact that the measured p-DIs of PCS cells exhibit greater pixel intensity variations in their patterns. Interestingly, the parameter ENT or entropy also gauges the degree of randomness in the intensity distributions of paired pixels but its values of calculated DIs are near the middle of the ranges of the measured DIs.

Among the selected GLCM parameters, IDM displays large value differences between the measured and calculated data in Figures 8 and 9. IDM is defined as the sum of p_{ij} with a weight that decreases as the intensity difference of

paired pixels or $(i-j)^2$ increases. This makes IDM very sensitive to the values of diagonal and near-diagonal elements in a GLCM. As a result, small IDM values indicate reduced numbers of pixel pairs having the same or similar intensities. One can observe that the measured DIs of co-polarized component in Figure 3, vertical-s or horizontal-p, exhibit wide-spread distributions of bright-dark spots over the full image field while the calculated DIs display large dark patches or pixel pairs of similarly low intensities in the peripheral areas. These results suggest that the calculated DIs have IDM values larger than or near the high end of the range by the measured DIs, which agree with the IDM plots in Figures 8 and 9 for both PC3-a and PCS-a structures. On the other hand, Figures 8 and 9 show that the OCMs developed in this report can yield DIs with MAP or maximum values of $\{p_{ij}\}$ that are similar to those of the measured data. We note here that other errors in the process of DI calculations can also cause the disagreement against the measured data, which include omission of intracellular organelles contributing to light scattering other than nucleus and mitochondria and inaccuracies in 3D reconstruction of cell structures for OCM.

4 | CONCLUSION

It is well known that rich information on 3D morphology can be extracted from spatial distributions of coherent light

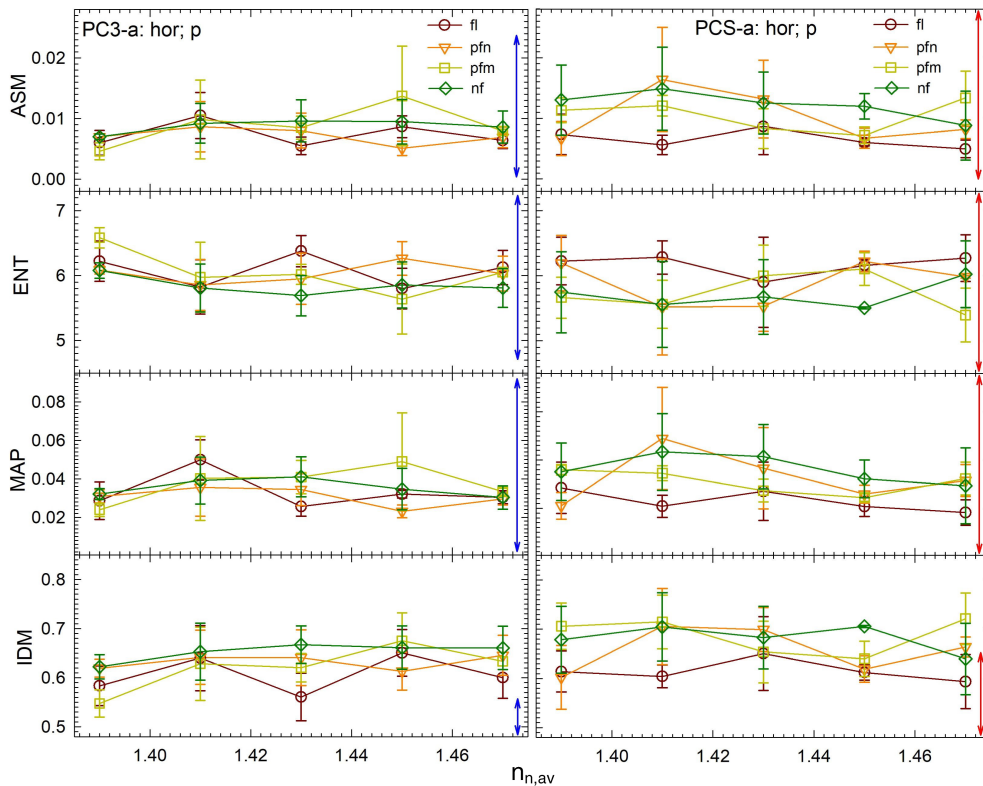


FIGURE 9 Same as Figure 8 except gray-level co-occurrence matrix (GLCM) parameters of p-polarized diffraction images (DIs) and horizontal incident polarization

scattered by microscopic particles in visible and near-infrared regions. Consequently single-shot imaging of scattered light intensity has strong potentials to become a powerful tool for rapid and label-free assay of single cells. Clear understanding of the relations between morphological features of imaged cells and diffraction patterns revealed by p-DI data is of fundamental importance and presents very challenging problems because of the highly heterogeneous cell structure and large variations even within the same phenotype. Development of a platform of realistic OCMs and validation approaches allows evaluation of OCMs through image data, which represents the first-step efforts to translate the methods of single-shot diffraction imaging into practical tools for label-free cell assay. In this report, we present a framework to build different realistic OCMs for simulation of diffraction imaging of live cells and evaluate them by comparing calculated p-DI pairs to the measured data with selected GLCM parameters and δ_L . It has been shown that nonspherical and highly irregular shapes of organelles in realistic OCMs are essential to obtain calculated p-DI pairs comparable to measured data of two prostate cell types. Detailed analysis of image intensity and textures by δ_L and GLCM reveals that the model parameters of n_{c0} , $n_{n,av}$ and $n_{m,av}$ have limited effects on diffraction patterns. Heterogeneity in RI distributions affects significantly the diffraction patterns for large RI values of nucleus. Still, the current realistic OCMs cannot generate calculated p-DI pairs with diffraction patterns and intensity ratios fully compatible to those of measured data for the prostate cells. OCM improvement with additional scattering relevant organelles such as lysosomes [6] is undertaken that will be evaluated with the framework presented here.

ACKNOWLEDGEMENTS

J.L. acknowledges grant support by the Science and Technology Program of Hunan Province (Nos.2016TP1021, 2018TP2022) and X.H. acknowledges grant support from Golfers Against Cancer (2012–13-GAC).

ORCID

Xin-Hua Hu  <https://orcid.org/0000-0002-4353-9028>

REFERENCES

- [1] S. J. Altschuler, L. F. Wu, *Cell* **2010**, *141*, 559.
- [2] B. Huang, M. Bates, X. Zhuang, *Annu. Rev. Biochem.* **2009**, *78*, 993.
- [3] E. M. Christiansen, S. J. Yang, D. M. Ando, A. Javaherian, G. Skibinski, S. Lipnick, E. Mount, A. O'Neil, K. Shah, A. K. Lee, P. Goyal, W. Fedus, R. Poplin, A. Esteve, M. Berndt, L. L. Rubin, P. Nelson, S. Finkbeiner, *Cell* **2018**, *173*, 792.
- [4] N. Lue, W. Choi, G. Popescu, K. Badizadegan, R. R. Dasari, M. S. Feld, *Opt. Express* **2008**, *16*, 16240.
- [5] W. Choi, C. Fang-Yen, K. Badizadegan, R. R. Dasari, M. S. Feld, *Opt. Lett.* **2008**, *33*, 171.
- [6] O. C. Marina, C. K. Sanders, J. R. Mourant, *Biomed. Opt. Express* **2012**, *3*, 296.
- [7] T. Kim, R. Zhou, M. Mir, S. D. Babacan, P. S. Carney, L. L. Goddard, G. Popescu, *Nat. Photonics* **2014**, *8*, 256.
- [8] M. Schürmann, J. Scholze, P. Müller, J. Guck, C. J. Chan, *J. Biophotonics* **2016**, *9*, 1068.
- [9] F. Merola, P. Memmolo, L. Miccio, R. Savoia, M. Mugnano, A. Fontana, G. D'Ippolito, A. Sardo, A. Iolascon, A. Gambale, P. Ferraro, *Light Sci. Appl.* **2017**, *6*, e16241.
- [10] Z. A. Steelman, W. J. Eldridge, J. B. Weintraub, A. Wax, *J. Biophotonics* **2017**, *10*, 1714.
- [11] A. C. Kak, M. Slaney, *Principles of Computerized Tomographic Imaging*, IEEE Press, New York, **1988**.
- [12] M. A. Yurkin, *J. Biophotonics* **2018**, *11*, e201800033.
- [13] J. Neukammer, C. Gohlke, A. Hope, T. Wessel, H. Rinneberg, *Appl. Optics* **2003**, *42*, 6388.
- [14] K. Singh, X. Su, C. Liu, C. Capjack, W. Rozmus, C. J. Backhouse, *Cytometry A* **2006**, *69*, 307.
- [15] L. Xie, Q. Liu, C. Shao, X. Su, *Opt. Express* **2017**, *25*, 29365.
- [16] D. K. Singh, C. C. Ahrens, W. Li, S. A. Vanapalli, *Lab Chip* **2017**, *17*, 2920.
- [17] K. M. Jacobs, J. Q. Lu, X. H. Hu, *Opt. Lett.* **2009**, *34*, 2985.
- [18] K. M. Jacobs, L. V. Yang, J. Ding, A. E. Ekpenyong, R. Castellone, J. Q. Lu, X. H. Hu, *J. Biophotonics* **2009**, *2*, 521.
- [19] Y. Sa, Y. Feng, K. M. Jacobs, J. Yang, R. Pan, I. Gkigkitzis, J. Q. Lu, X. H. Hu, *Cytometry A* **2013**, *83*, 1027.
- [20] Y. Feng, N. Zhang, K. M. Jacobs, W. Jiang, L. V. Yang, Z. Li, J. Zhang, J. Q. Lu, X. H. Hu, *Cytometry A* **2014**, *85*, 817.
- [21] H. Wang, Y. Feng, Y. Sa, Y. Ma, R. Pan, J. Q. Lu, X. H. Hu, *Appl. Optics* **2015**, *54*, 5223.
- [22] K. Dong, Y. Feng, K. M. Jacobs, J. Q. Lu, R. S. Brock, L. V. Yang, F. E. Bertrand, M. A. Farwell, X. H. Hu, *Biomed. Opt. Express* **2011**, *2*, 1717.
- [23] X. Yang, Y. Feng, Y. Liu, N. Zhang, W. Lin, Y. Sa, X. H. Hu, *Biomed. Opt. Express* **2014**, *5*, 2172.
- [24] W. Jiang, J. Q. Lu, L. V. Yang, Y. Sa, Y. Feng, J. Ding, X. H. Hu, *J. Biomed. Opt.* **2016**, *21*, 071102.
- [25] H. Wang, Y. Feng, Y. Sa, J. Q. Lu, J. Ding, J. Zhang, X.-H. Hu, *Pattern Recognit.* **2016**, *61*, 234.
- [26] W. Wang, J. Liu, J. Q. Lu, J. Ding, X. H. Hu, *Opt. Express* **2017**, *25*, 9628.
- [27] C. Liu, C. Capjack, W. Rozmus, *J. Biomed. Opt.* **2005**, *10*, 14007.
- [28] A. Zharinov, P. Tarasov, A. Shvalov, K. Semyanov, D. R. van Bockstaele, V. P. Maltsev, *J. Quant. Spectrosc. Radiat. Transf.* **2006**, *102*, 121.
- [29] X.-T. Su, C. Capjack, W. Rozmus, C. Backhouse, *Opt. Express* **2007**, *15*, 10562.
- [30] D. Y. Orlova, M. A. Yurkin, A. G. Hoekstra, V. P. Maltsev, *J. Biomed. Opt.* **2008**, *13*, 054057.
- [31] L. Zhang, Y. Qin, K.-X. Li, X. Zhao, Y.-F. Xing, H. Zhao, Z. Jiang, W. Chen, N.-L. Yao, L. Yuan, *Opt. Quant. Electron.* **2015**, *47*, 1005.
- [32] H. Shahin, M. Gupta, A. Janowska-Wieczorek, W. Rozmus, Y. Y. Tsui, *Opt. Express* **2016**, *24*, 28877.
- [33] J. Stark, T. Rothe, S. Kiess, S. Simon, A. Kienle, *Phys. Med. Biol.* **2016**, *61*, 2749.
- [34] X. Lin, N. Wan, L. Weng, Y. Zhou, *Appl. Optics* **2017**, *56*, 3608.
- [35] R. S. Brock, X. H. Hu, P. Yang, J. Q. Lu, *Opt. Express* **2005**, *13*, 5279.
- [36] J. Q. Lu, P. Yang, X. H. Hu, *J. Biomed. Opt.* **2005**, *10*, 024022.
- [37] D. I. Strokotov, A. E. Moskalensky, V. M. Nekrasov, V. P. Maltsev, *Cytometry A* **2011**, *79A*, 570.
- [38] K. V. Gilev, M. A. Yurkin, E. S. Chernyshova, D. I. Strokotov, A. V. Chernyshev, V. P. Maltsev, *Biomed. Opt. Express* **2016**, *7*, 1305.
- [39] A. E. Moskalensky, M. A. Yurkin, A. R. Muliukov, A. L. Litvienko, V. M. Nekrasov, A. V. Chernyshev, V. P. Maltsev, *PLoS Comput. Biol.* **2018**, *14*, e1005899.
- [40] R. S. Brock, X. H. Hu, D. A. Weidner, J. R. Mourant, J. Q. Lu, *J. Quant. Spectrosc. Radiat. Transf.* **2006**, *102*, 25.
- [41] Y. Zhang, Y. Feng, C. R. Justus, W. Jiang, Z. Li, J. Q. Lu, R. S. Brock, M. K. McPeck, D. A. Weidner, L. V. Yang, X. H. Hu, *Integr. Biol.* **2012**, *4*, 1428.
- [42] J. Zhang, Y. Feng, W. Jiang, J. Q. Lu, Y. Sa, J. Ding, X. H. Hu, *Opt. Express* **2016**, *24*, 366.
- [43] R. Pan, Y. Feng, Y. Sa, J. Q. Lu, K. M. Jacobs, X. H. Hu, *Opt. Express* **2014**, *22*, 31568.

- [44] M. A. Yurkin, A. G. Hoekstra, *J. Quant. Spectrosc. Radiat. Transf.* **2011**, *112*, 2182.
- [45] Y. Wen, Z. Chen, J. Lu, E. Ables, J. L. Scemama, L. V. Yang, J. Q. Lu, X. H. Hu, *PLoS One* **2017**, *12*, e0184726.
- [46] J. D. Wilson, C. E. Bigelow, D. J. Calkins, T. H. Foster, *Biophys. J.* **2005**, *88*, 2929.
- [47] M. Kalashnikov, W. Choi, C.-C. Yu, Y. Sung, R. R. Dasari, K. Badizadegan, M. S. Feld, *Opt. Express* **2009**, *17*, 19674.
- [48] R. M. Haralick, *Proc. IEEE* **1979**, *67*, 786.
- [49] X. H. Hu, 3D Morphology and GLCM Parameter Definition Tables, http://bmlaser.physics.ecu.edu/literature/3D_GLCM_Para_Def_Tables.pdf, accessed on 10 August 2018
- [50] M. I. Mishchenko, J. W. Hovenier, *Opt. Lett.* **1995**, *20*, 1356.
- [51] K. H. Zou, K. Tuncali, S. G. Silverman, *Radiology* **2003**, *227*, 617.
- [52] Y. Sa, J. Zhang, M. S. Moran, J. Q. Lu, Y. Feng, X. H. Hu, *Opt. Express* **2012**, *20*, 22245.

How to cite this article: Wang S, Liu J, Lu JQ, et al. Development and evaluation of realistic optical cell models for rapid and label-free cell assay by diffraction imaging. *J. Biophotonics*. 2019;12:e201800287. <https://doi.org/10.1002/jbio.201800287>